Journal of Power Sources 195 (2010) 7003–7010

Contents lists available at ScienceDirect

Journal of Power Sources

journal homepage: www.elsevier.com/locate/jpowsour

Phase change in the cathode side of a proton exchange membrane fuel cell

N. Khajeh-Hosseini-Dalasm*, Kazuyoshi Fushinobu, Ken Okazaki

Department of Mechanical and Control Engineering, Tokyo Institute of Technology, Meguro-ku, Tokyo 152-8552, Japan

ARTICLE INFO

Article history:
Received 25 February 2010
Received in revised form 19 April 2010
Accepted 30 April 2010
Available online 13 May 2010

Keywords:
PEM fuel cell
Non-equilibrium phase change
Two-phase flow
Porous electrode
Non-isothermal
Operating conditions

ABSTRACT

A three-dimensional steady state two-phase non-isothermal model which highly couples the water and thermal management has been developed to numerically investigate the spatial distribution of the interfacial mass transfer phase-change rate in the cathode side of a proton exchange membrane fuel cell (PEMFC). A non-equilibrium evaporation–condensation phase change rate was incorporated in the model which allowed supersaturation and undersaturation take place. The most significant effects of phase-change rate on liquid saturation and temperature distributions are highlighted. A parametric study was also carried out to investigate the effects of operating conditions; namely as the channel inlet humidity, cell operating temperature, and inlet mass flow rate on the phase-change rate. It was also found that liquid phase assumption for produced water in the cathode catalyst layer (CL) changed the local distribution of phase-change rate. The maximum evaporation rate zone (above the channel near the CL) coincided with the maximum temperature zone and resulted in lowering the liquid saturation level. Furthermore, reduction of the channel inlet humidity and an increase of the operation temperature and inlet mass flow rate increased the evaporation rate and allowed for dehydration process of the gas diffusion layer (GDL) to take place faster.

1. Introduction

Two of the most critical topics in proton exchange membrane fuel cell (PEMFC) modeling are water and thermal management. In several studies, these two topics are addressed separately and the couple water-thermal management has been neglected. Since vapor pressure is a strong function of temperature, decoupling of water and thermal management is inaccurate. When the water management is studied and the thermal management is neglected, for instance in isothermal models, the effect of thermally driven vapor phase transport and change is not considered. On the other hand, when the thermal management is studied and the water management is neglected, for instance in single phase models, liquid water flooding and the resulting mass transport limitation are neglected.

Phase-change, evaporation–condensation processes, has the most significant role in the coupling of water and thermal management. This phenomenon is more significant in the porous gas diffusion layer (GDL) where the main mechanism of mass transport is diffusion. Phase-change is included with heat source (or sink) and liquid water source (or sink). Consequently, it changes the fuel cell performance by changing the liquid water flooding level and temperature variation.

Several two-phase studies have been reported [1–29]. To the best of the authors' knowledge, only some of them have investigated directly the phase-change rate and its effects. Basu et al. [25] studied the three-dimensional phase-change in a PEMFC using a two-phase mixture model while assuming thermodynamic equilibrium. It was assumed that the partial pressure of water vapor is equal to the saturated vapor pressure (thermodynamic equilibrium) and with this assumption the liquid saturation was obtained from the definition of total water concentration (in the post-processing stage). Although this assumption results in a zero phase-change rate when a non-equilibrium phase-change is assumed. In their study, phase-change rate was obtained from the divergence of the phase velocity in the post-processing stage. Furthermore, it was assumed that water is produced in the vapor phase in the cathode catalyst layer (CL). In a two-dimensional configuration, Meng [15] employed a two-phase two-fluid model with a non-equilibrium phase-change rate. The amounts of the condensation and evaporation constants were determined using the assumption that at high operating temperature and inlet humidity there was no evaporation. However, the channel effect was not considered, and the water phase produced in CL is assumed to be vapor.

In this paper, a three-dimensional steady-state two-phase non-isothermal model is presented for the cathode side of a PEMFC which strongly couples water management and

* Corresponding author. Tel.: +81 3 5734 2179; fax: +81 3 5734 2179.
E-mail addresses: khajehhosseini.n.aa@m.titech.ac.jp (N. Khajeh-Hosseini-Dalasm), fushinobu.k.aa@m.titech.ac.jp (K. Fushinobu), okazaki.k.aa@m.titech.ac.jp (K. Okazaki).

0378-7753/$ – see front matter © 2010 Elsevier B.V. All rights reserved.
doi:10.1016/j.jpowsour.2010.04.089

Nomenclature

A	area (m^2)
c_p	specific heat ($J\,kg^{-1}\,K^{-1}$)
D	diffusion coefficient ($m^2\,s^{-1}$)
E	voltage (V)
F	Faraday constant (96,485 $C\,mol^{-1}$)
h	latent heat of evaporation ($J\,kg^{-1}$)
i	local current density ($A\,cm^{-2}$)
I	cell current density ($A\,cm^{-2}$)
j	transfer current density ($A\,cm^{-3}$)
$J(s)$	Leverett function
k	thermal conductivity ($W\,m^{-1}\,K^{-1}$)
k_{cond}	condensation rate constant (s^{-1})
k_{evap}	evaporation rate constant ($Pa^{-1}\,s^{-1}$)
k_r	relative permeability
K	hydraulic permeability
$\dot{m}$	interfacial phase change mass transfer rate ($kg\,m^{-3}\,s^{-1}$)
M	molecular weight ($kg\,mol^{-1}$)
P	pressure (Pa)
r	Ohmic resistance ($\Omega\,m^2$)
$\bar{R}$	universal gas constant (8.314 $J\,mol^{-1}\,K^{-1}$)
s	liquid saturation
Δs	entropy change ($J\,mol^{-1}\,K^{-1}$)
S	source term ($W\,m^{-3}\,s^{-1}$)
T	temperature (K)
V	velocity ($m\,s^{-1}$)
$\forall$	volume of the control volume (m^3)
x, y, z	coordinate (m)
X	mole fraction
Y	mass fraction

Greek letters

α	transport coefficient
ε	porosity
η	activation overpotential (V)
θ	contact angle (rad)
λ	mobility
μ	dynamic viscosity ($kg\,m^{-1}\,s^{-1}$)
ν	kinematic viscosity ($m^2\,s^{-1}$)
ρ	density ($kg\,m^{-3}$)
σ	conductivity ($S\,m^{-1}$)
τ	surface tension ($N\,m^{-1}$)

Superscripts and subscripts

c	cathode side
$cond$	condensation
C	capillary
eff	effective
$evap$	evaporation
fg	phase change
g	gas phase
H_2O	water
i	species i
in	inlet
l	liquid phase
O_2	oxygen
r	relative
ref	reference
s	solid phase
sat	saturation state
T	thermal

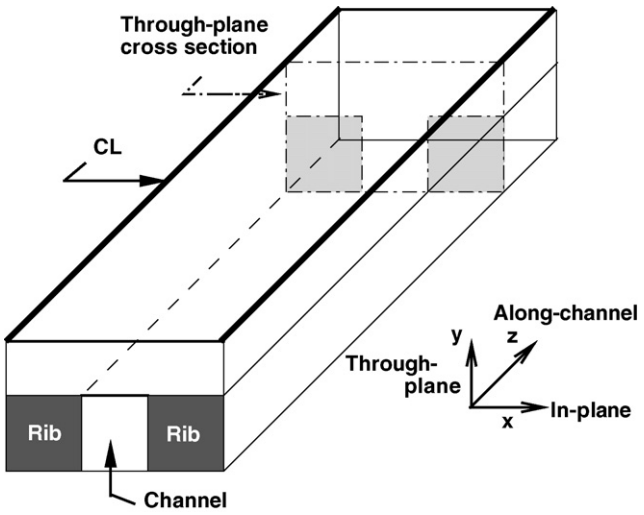

Fig. 1. Schematic of the model and a through-plane cross-section.

thermal management through the liquid–vapor phase-change (evaporation–condensation) rate. The most significant effects of the interfacial phase-change rate in fuel cell operation have been investigated by exploring its effect on the saturation level and temperature variation. Moreover, a parametric study is carried out by changing the gas channel inlet humidity, operating temperature, and inlet gas flow rate to clarify the role of phase-change in the fuel cell performance. A non-equilibrium phase-change rate is also considered that allows for supersaturation and undersaturation to take place. The governing equations are developed for the two-phase mixture (gas and liquid phases) while for each phase its corresponding conservation equation is incorporated. The partial differential equations resulting from the governing equations are discretized by the control volume method and a FORTRAN code has been developed to accomplish the numerical simulation. It is believed that this study can help understanding the role of the phase-change in a PEMFC operation. It also gives guidelines for design optimization of a PEMFC.

2. Governing equations

The three-dimensional computational domain has been sketched in Fig. 1. The domain represents the cathode side of a PEMFC consisting of the ribs, gas channel, GDL and CL. The inlet gas mixture which is humid oxygen gas is fed into the channel. The reactant diffuses through the porous GDL and reaches to the reaction site in CL. The CL is treated as an interface and the electrochemical reaction, i.e. oxygen reduction reaction (ORR) takes place at the GDL/CL interface. In Fig. 1, a through-plane cross-section is also shown. The through-plane cross- section is used to present the results.

In the present numerical study, the phase-change rate, evaporation and condensation rates, in the porous GDL studied. The governing equations describe a three-dimensional steady state two-phase non-isothermal model. The governing equations listed below include: conservation of mass, momentum, water vapor species, liquid water and energy.

Conservation of mass

$$\nabla \cdot (\varepsilon \rho \vec{V}) = 0 \tag{1}$$

Conservation of momentum

$$\nabla \cdot (\varepsilon \rho \vec{V}\,\vec{V}) = -\varepsilon \nabla P + \nabla \cdot (\varepsilon \mu \nabla \vec{V}) - \frac{\varepsilon^2 \mu}{K} \vec{V} \tag{2}$$

Table 1
Constitutive relations.

Parameters	Expressions
Two-phase mixture density	$\rho = s\rho_l + (1-s)\rho_g$
The gas phase density	$\rho_g = \frac{PM_g}{RT}$
Gas mixture molecular weight	$M_g = \left(\sum_i \frac{Y_g^i}{M_g^i}\right)^{-1}$
Two-phase mixture dynamic viscosity	$\mu = \frac{s\rho_l + (1-s)\rho_g}{\rho_l k_{rl}/\mu_l + \rho_g k_{rg}/\mu_g}$
Liquid water dynamic viscosity	$\mu_l = 0.6612(T-229)^{-1.562}$
The relative permeabilities	$k_{rl} = s^3, \quad k_{rg} = (1-s)^3$
Mole fraction and mass fraction	$X_i = Y_i \frac{M_g}{M_i}$
Saturated vapor pressure	$\log_{10} P_{sat} = -2.1794 + 0.02953(T-273) - 9.1837\times10^{-5}(T-273) + 1.4454\times10^{-7}(T-273)^3$
Liquid phase mobility	$\lambda_l = \frac{\rho_l k_{rl}/\mu_l}{\rho_l k_{rl}/\mu_l + \rho_g k_{rg}/\mu_g}$
Gas phase mobility	$\lambda_g = 1 - \lambda_l$
Capillary pressure	$P_C = \tau\cos(\theta_c)\left(\frac{\varepsilon}{K}\right)^{1/2} J(s)$
Leverett function	$J(s) = \begin{cases} \theta_c < 90^\circ \\ 1.417(1-s) - 2.210(1-s)^2 + 1.263(1-s)^3 \\ \theta_c > 90^\circ \\ 1.417s - 2.210s^2 + 1.263s^3 \end{cases}$
Effective diffusion coefficient	$D_g^{H_2O,eff} = (\varepsilon(1-s))^{1.5} D_g^{H_2O,O_2}$
	$\rho c_p = s\rho_l c_{p,l} + (1-s)\rho_g c_{p,g}$
Effective thermal conductivity	$k^{eff} = \varepsilon s k_l + \varepsilon(1-s)k_g + (1-\varepsilon)k_s$
Specific heat of gas mixture	$c_{p,g} = \sum_i X_i c_{p,i}$
Thermal conductivities	$k_{O_2} = 0.223\times10^{-3}T^{0.839}$, $k_{H_2O} = 0.0025\times10^{-3}T^{1.56}$
Latent heat of phase change	$h_{fg} = 3.0709\times10^5(647.15-T)^{0.35549}$
Reversible cell voltage	$E_{rev} = 0.0025\times T + 0.2329$

Conservation of water vapor

$$\nabla\cdot(\varepsilon(1-s)\rho_g\vec{V}_g Y_g^{H_2O}) = \nabla\cdot(\varepsilon(1-s)\rho_g D_g^{H_2O,eff}\nabla Y_g^{H_2O}) - \varepsilon\dot{m}_l \quad (3)$$

Conservation of liquid water

$$\nabla\cdot\left(\rho K\frac{\lambda_l\lambda_g}{\mu}\frac{\partial P_C}{\partial s}\nabla s + \varepsilon\lambda_l\rho\vec{V}\right) = \varepsilon\dot{m}_l \quad (4)$$

Conservation of energy

$$\nabla\cdot(\rho(\lambda_l c_{p,l} + \lambda_g c_{p,g})\vec{V}T) = \nabla\cdot(k^{eff}\nabla T) + S_T \quad (5)$$

The main variables in the above set of governing equations are: the two-phase mixture density ρ, the mass-averaged mixture velocity vector $\vec{V}$ (three components), the mass fraction of water vapor $Y_g^{H_2O}$, the liquid saturation s and the temperature T. In order to close the system of governing equations, a set of constitutive relations are needed. These relations are listed in Table 1.

In Eq. (4) presented for the liquid water conservation, $\dot{m}_l$ indicated the interfacial mass transfer phase-change rate. Phase-change takes place inside the domain when the water vapor concentration is higher or less than the saturated water vapor concentration. A non-equilibrium phase-change rate is incorporated in the present model. In contrast with a thermodynamic equilibrium assumption, the non-equilibrium phase-change rate allows the local departures from saturation state which means it allows a supersaturation and undersaturation to take place. The non-equilibrium phase changes rates are expresses as [7]

$$\dot{m} = \begin{cases} k_{cond}(1-s)(M^{H_2O}/\bar{R}T)P(X_g^{H_2O} - X_{sat}^{H_2O}), & X_g^{H_2O} \geq X_{sat}^{H_2O} \\ k_{evap}s\rho_l P(X_g^{H_2O} - X_{sat}^{H_2O}), & X_g^{H_2O} < X_{sat}^{H_2O} \end{cases} \quad (6)$$

The mass transferred from a vapor–liquid phase interface is related to the departure from saturation state through the condensation and evaporation rates constants, respectively shown by k_{cond} and k_{evap}. The values of these constants are adopted from Ref. [11].

In the derivation of the conservation equation for energy, a thermal equilibrium among the three existing phases, i.e. solid, gas and liquid has been made. The source term in the energy equation Eq. (5) is shown by S_T. Inside the domain where the phase-change takes place the energy source term includes the latent heat of vapor–liquid phase change

$$S_T = \varepsilon\dot{m}h_{fg} \quad (7)$$

Heat is released where condensation takes place ($\dot{m}$ is a positive value) and is absorbed where evaporation takes place ($\dot{m}$ is a negative value).

The energy source term in the CL is given by

$$S_T = j\frac{T\Delta s}{2F} + j\eta + \frac{i}{\sigma_e^{eff}} + \frac{i}{\sigma_p^{eff}} \quad (8)$$

where j (A cm^{-3}) and i (A cm^{-2}) are the transfer current density and local current density, respectively. Δs is the entropy change of the ORR; considering the liquid phase for water produced as a result of the ORR. η shows the activation overpotential. σ_e^{eff} and σ_p^{eff} denote the electronic and protonic conductivities, respectively (see Ref. [29] for the values).

2.1. Electrochemical kinetics and cell voltage

The oxygen reduction reaction takes place in the cathode catalyst layer; as a result, current is generated in the catalyst layer. The generated current density named as local current density in the CL/GDL interface is calculated via the Butler–Volmer equation describing the kinetics of the reaction

$$i = i_0(1-s)\left(\frac{Y_g^{O_2}}{Y_g^{O_2,ref}}\right)\exp\left(\frac{\alpha_c F}{\bar{R}T}\eta\right) \quad (9)$$

Table 2
Geometrical and operational parameters.

Parameters	Notation	Value
Geometrical parameters		
Channel width (m)	–	1.3×10^{-3}
Channel height (m)	–	1×10^{-3}
GDL thickness (m)	–	3.8×10^{-4}
Channel length (m)	–	2×10^{-2}
CL thickness (m)	l_c	1×10^{-5}
Operational properties		
Temperature (K)	T_{in}	353
Inlet pressure (atm)	P	1
Inlet humidity	ϕ_{in}	10%
Inlet gas flow rate ($m^3\ s^{-1}$)	q	8.3×10^{-7}
Transport properties		
Universal molar gas constant ($J\ mol^{-1}\ K^{-1}$)	$\bar{R}$	8.314
Reversible cell voltage (V)	E_{rev}	1.115
Binary diffusion coefficient ($m^2\ s^{-1}$)	$D_g^{H_2O,O_2}$	3.76×10^{-5}
Viscosity of liquid water ($kg\ m^{-1}\ s^{-1}$)	μ_l	3.5×10^{-4}
Liquid water density ($kg\ m^{-3}$)	ρ_l	998
Entropy change at the inlet temperature ($J\ mol^{-1}\ K^{-1}$)	ΔS	163.7
Condensation rate constant (s^{-1})	k_{cond}	100
Evaporation rate constant ($Pa^{-1}\ s^{-1}$)	k_{evap}	9.8×10^{-6}
Structural properties		
Porous electrode porosity	ε	0.4
Hydraulic permeability of GDL (m^2)	K	1.76×10^{-11}
Surface tension, liquid water and air ($N\ m^{-1}$)	σ	0.062
Contact angle	θ_c	110

where i_0 and $Y_g^{O_2,ref}$ are the exchange current density and reference oxygen mass fraction, respectively. η is the activation overpotential. The parameters α_c and F represent the cathode side transfer coefficient and Faraday constant. It is noted that in the present study the activation overpotential is fixed; therefore, local current density can be obtained using Eq. (9). The average current density is obtained by integration of the local current density in the CL interface as

$$I = \frac{1}{A}\int_{\Delta x}\int_{\Delta z} i\,dz\,dx \tag{10}$$

where A is the surface area of the CL. Finally, the cell voltage can be determined from

$$E_{cell} = E_{rev} - \eta - rI \tag{11}$$

where E_{rev}, r and I are the reversible cell voltage, ohmic resistance and average current density, respectively.

The governing equations for mass, momentum, species, and energy yield a system of partial differential equations with seven main unknowns, i.e. P, three components of velocity vector $\vec{V}$, $Y_g^{H_2O}$, s and T. Other parameters (listed in Table 1) can be calculated using these unknowns. The computational domain geometry and the operational, physical and electrochemical properties used in this numerical simulation have been listed in Table 2. In order to be able to solve the three-dimensional governing equations, a suitable set of boundary conditions is also needed and will be explained in the next section.

3. Boundary conditions

For explaining the boundary conditions, the computational domain shown in Fig. 1 is recalled. This domain is a part taken from a complete cell and shows a single cell straight channel domain. A symmetry boundary condition along the x-axis is specified for the vector and scalar main unknowns. The inlet flow is humidified oxygen gas and is assumed that there in no liquid water droplet in the inlet flow. Along the channel, i.e. z-axis direction, the inlet velocity is obtained from the inlet gas flow rate q ($m^3\ s^{-1}$) and inlet cross-sectional area A (m^2)

$$w_{in} = \frac{q}{A} \tag{12}$$

The oxygen mass fraction in the inlet humid gas mixture can be calculated as

$$Y_{g,in}^{O_2} = \left(1 - \frac{\phi_{in}P_{sat}}{P}\right)\frac{M_g^{O_2}}{M_g} \tag{13}$$

where ϕ_{in} is the inlet humidity. The inlet temperature T_{in} is constant and equal to the cell operating temperature. For the outlet flow, a laminar fully developed flow is assumed which is reasonable for the small flow velocity in the channel. The gradient of the main unknowns at the outlet is assumed to be zero, therefore there is no changes for their values.

In the through-plane direction, i.e. y-axis the button surface is a solid wall. A no-slip condition for velocity vector is specified as well as a constant temperature equal to the operating temperature. For other scalar quantities a zero gradient normal to the surface is identified. The upper surface is the CL interface and the boundary conditions are developed by applying the surface fluxes of the liquid water production, oxygen consumption and released thermal energy in the CL. More details can be found in Khajeh-Hosseini-Dalasm et al. [30].

4. Numerical solution procedure

The nonlinear partial differential governing equations, Eqs. (1)–(5) which constitute the present three- dimensional steady state two-phase non-isothermal study are solved numerically using the corresponding boundary conditions explained in Section 3. The governing equations along with the boundary conditions are discretized by finite volume method (FVM) and the SIMPLE algorithm [31,32] is employed to deal with the pressure linked flow field. A FORTRAN code is developed in order to accomplish the numerical simulation. A precise convergence criterion is used in which both the relative error of each main unknown between two consecutive iterations and the residual of discretization are checked. Furthermore, mesh independency of solution was confirmed.

5. Results and discussion

In this paper, the spatial distribution of the phase-change rate is studied first. The results are presented at a fixed average current density equal to $1.5\ A\ cm^{-2}$. The fixed average current density leads to constant liquid water and heat fluxes for all the case studies conducted in this paper. Therefore, the liquid saturation and temperature variations inside the domain are associated mostly with the phase-change rate quantity and distribution. Next, a parametric study is carried out by changing the gas channel inlet humidity, operation temperature, and inlet gas flow rate to explore how the phase-change rate is affected by these operating conditions. Finally, the effects of phase-change rate on the liquid saturation level and temperature distribution are highlighted.

Fig. 2 shows the interfacial mass transfer phase-change rate $kg\ m^{-3}\ s^{-1}$ in a through-plane cross-section located at near the outlet, i.e. $z/z_L = 0.9$ where z_L is the total length of the channel. The operating temperature is 353 K (80 °C), channel inlet humidity is 10%, and the inlet gas flow rate is $8.3 \times 10^{-7}\ m^3\ s^{-1}$ (50 sccm). Hereafter, these conditions are named as the base case condition. In Fig. 2, positive and negative contour values denote condensation

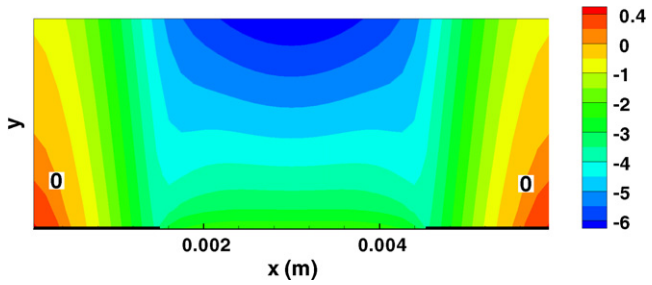

Fig. 2. Through-plane distribution of the interfacial phase-change rate (kg m^{-3} s^{-1}) in the cathode porous GDL when $T = 353$ K, $\phi = 10\%$, and $q = 8.3 \times 10^{-7}$ m^3 s^{-1}.

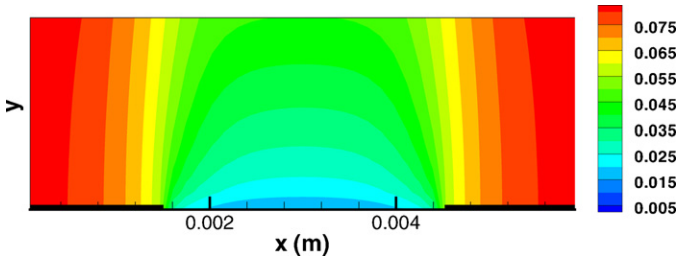

Fig. 4. Through-plane distribution of liquid saturation in the cathode porous GDL when $T = 353$ K, $\phi = 10\%$, and $q = 8.3 \times 10^{-7}$ m^3 s^{-1}.

and evaporation, respectively. For the base case simulation conducted in Fig. 2, the inlet humidity and gas flow rate are relatively low, but operating temperature is relatively high; it is seen that most of the evaporation takes place in the GDL while only two small regions above the ribs show condensation of water vapor. Moreover, the maximum evaporation rate is around 12 times higher than the maximum condensation rate. It can be also found that the maximum evaporation rate occurs above the channel near the CL while the maximum condensation rate occurs above and near the ribs. The evaporation front, the boundary between the evaporation and condensation regions, is specified by the contour value of zero phase change rate. This shows that in the base case, the evaporation front has penetrated deep inside the GDL.

The non-equilibrium phase change in Eq. (6) allow supersaturation and undersaturation take place. The bigger the departure of water vapor pressure, P_{H_2O}, from the saturated vapor pressure, P_{sat}, the higher the phase-change rate. Supersaturation, $\phi > 1$, leads to condensation and undersaturation, $\phi < 1$, leads to evaporation. The relative humidity (ϕ) distribution inside the GDL for the base case condition is plotted in Fig. 3. In agreement with Fig. 2, Fig. 3 shows the highest undersaturation above the channel near the CL and the highest supersaturation above and near the ribs. The amount of supersaturation is insignificant. However, in the two-phase mixture modeling approach, in the two-phase zone always the relative humidity is 1 (or 100%) and the existence of both liquid and vapor phases at the relative humidity not equal to 1 is impossible.

In Fig. 2, it is seen that the region in the vicinity of the CL undergoes evaporation. This is due to the higher temperature which will be illustrated in the later results. This observation is different from the results obtained by Basu et al. [25]. They employed a multiphase mixture model and assumed that the water is produced in the vapor phase in the CL as a result of ORR. A condensation zone was observed above the ribs near the CL even at low inlet humidity. The effect of liquid or vapor phases assumption for water produced in the CL due to ORR was addressed by Wu et al. [26]. It was concluded that the transient time was longer when the water vapor phase was assumed. In the present study, another difference is addressed which is the different local distribution of the phase-change rate.

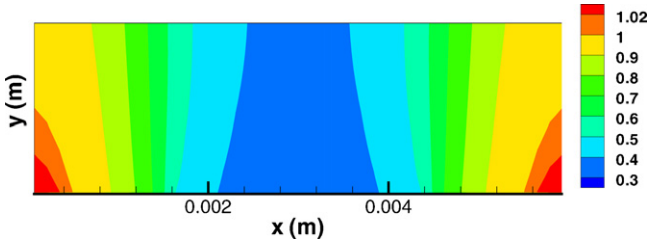

Fig. 3. Through-plane distribution of relative humidity in the cathode porous GDL when $T = 353$ K, $\phi = 10\%$, and $q = 8.3 \times 10^{-7}$ m^3 s^{-1}.

In the following, the corresponding liquid saturation and temperature distributions to the base case condition, shown in Fig. 2, are presented. Fig. 4 shows the liquid saturation distribution for the base case condition. The entire GDL at the steady state condition is partially flooded by liquid water. The existence of liquid water is necessary for the evaporation process inside the GDL (see s in Eq. (6)). It is seen that the liquid water is maximum above the ribs, while the minimum liquid saturation is above and close to the channel. The higher liquid saturation above the channel near the CL compared to near the channel is due to liquid water removal to the channel and evaporation process. Moreover, it is noted that the through-plane liquid saturation gradient above the ribs is much less than that of above the channel. This is illustrated in Fig. 5 where the in-plane profiles of liquid saturation are plotted at different heights of the GDL. The non-dimensional distance, Y^*, from the channel/GDL interface is defined as y/y_L where y_L is the GDL thickness.

The corresponding temperature distribution for the base case condition is displayed in Fig. 6. It shows the temperature distribution in the channel and porous GDL. The maximum temperature is above the channel near the CL. This corresponds to the higher current generated in the CL, due to lower diffusion resistance and higher oxygen concentration. While the minimum temperature zones in the GDL are seen above the ribs.

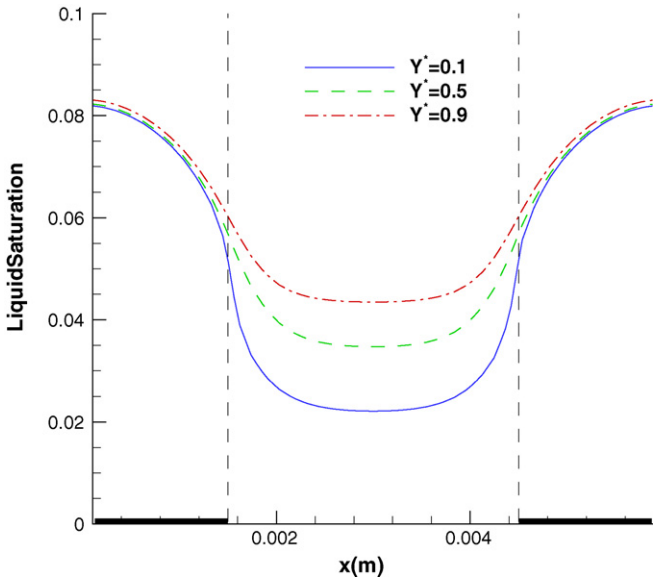

Fig. 5. In-plane profiles of liquid saturation in the cathode porous layer when $T = 353$ K, $\phi = 10\%$, and $q = 8.3 \times 10^{-7}$ m^3 s^{-1} at different through-plane heights.

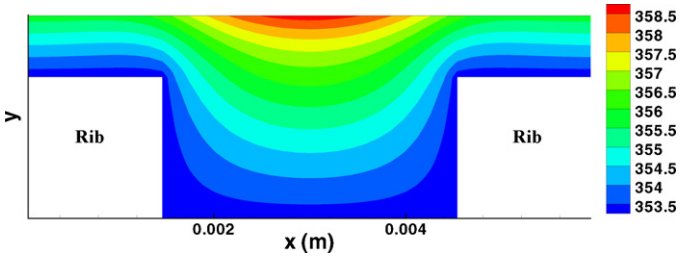

Fig. 6. Through-plane distribution of temperature in the cathode side when $T = 353$ K, $\phi = 10\%$, and $q = 8.3 \times 10^{-7}$ m^3 s^{-1}.

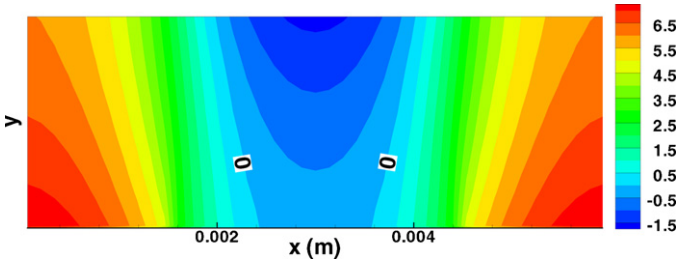

Fig. 7. Through-plane distribution of interfacial phase-change rate (kg m^{-3} s^{-1}) in the cathode porous GDL when $T = 353$ K, $\phi = 100\%$, and $q = 8.3 \times 10^{-7}$ m^3 s^{-1}.

5.1. Effects of gas channel inlet relative humidity

For the base case the inlet relative humidity is 10% where it is observed that evaporation occurs mostly inside the GDL. Fig. 7 represents the through-plane distribution of the interfacial mass transfer phase-change rate kg m^{-3} s^{-1} at the base case condition but with a fully humidified inlet flow ($\phi = 100\%$). It is remembered here that the positive contour values denote condensation and the negative values denote evaporation. In comparison with inlet relative humidity of 10% (Fig. 2), it can be seen that a vast area is subject to condensation. This is due to the increased relative humidity inside the domain by supplying fully humidified reactant into the channel. Higher humidity increases the degree of supersaturation, therefore the condensation process is accelerated and expanded inside the GDL. The degree of supersaturation and undersaturation is demonstrated by presenting the relative humidity distribution in Fig. 8. The condensation rate is around 18 times higher than the low inlet humidity case shown in Fig. 2. The evaporation rate is negligible expect for a small area in the vicinity of the CL above the channel. The maximum condensation rate (above the ribs) is more than 4 times higher than the maximum evaporation rate.

5.2. Effects of operating temperature

The effects of reducing the operating temperature on the phase-change rate are investigated in the following section. Fig. 9 displays the through-plane distribution of the interfacial mass transfer phase-change rate kg m^{-3} s^{-1} for the same conditions as the base

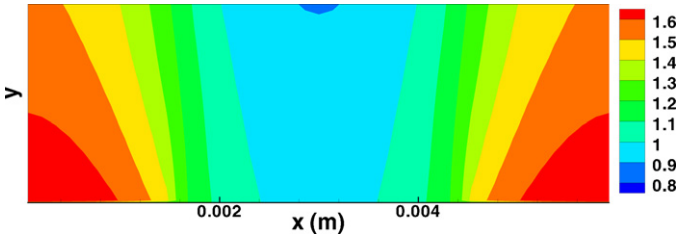

Fig. 8. Through-plane distribution of relative humidity in the cathode porous GDL when $T = 353$ K, $\phi = 100\%$, and $q = 8.3 \times 10^{-7}$ m^3 s^{-1}.

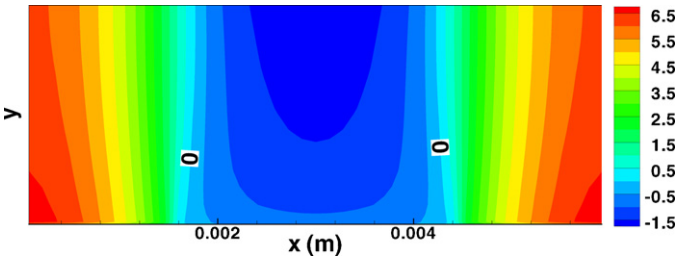

Fig. 9. Through-plane distribution of interfacial phase-change rate (kg m^{-3} s^{-1}) in the cathode porous GDL when $T = 333$ K, $\phi = 10\%$, and $q = 8.3 \times 10^{-7}$ m^3 s^{-1}.

case except for the operating temperature which is reduced to 333 K (60 °C). In comparison with the base case in Fig. 2, it is seen that at the lower operating temperature the condensation phase change process is accelerated and more developed toward the middle of the channel. The phase change rate is strongly related on the temperature since the saturated vapor pressure strongly depends on temperature (see Table 1 for P_{sat}). The 20 ° C reduction in the operating temperature from 353 K to 333 K leads to a 57% reduction of the saturated vapor pressure. As expected from this big change in saturated vapor pressure, the phase-change rate is also different. The maximum condensation rate increases up to 10 times and the evaporation rate decreases up to 3 times.

5.3. Effects of inlet gas flow rate

The effect of the channel inlet gas flow rate on the phase-change rate is investigated by increasing the inlet gas flow rate fed into the channel. Fig. 10 represents the through-plane distribution of the interfacial mass transfer phase-change rate kg m^{-3} s^{-1} for the same condition as the base case except for the inlet gas flow rate is increased to $q = 50 \times 10^{-7}$ m^3 s^{-1} (300 sccm). Compared to the lower inlet gas flow rate case shown in Fig. 2, it is seen that the entire GDL is under the evaporation (even above the ribs). Increasing the inlet mass flow rate from $q = 8.33 \times 10^{-7}$ m^3 s^{-1} (50 sccm) at the base case to $q = 50 \times 10^{-7}$ m^3 s^{-1} (300 sccm) leads to an increase of inlet velocity with the same order (6 times higher) (see Eq. 12). The inlet velocity is changed from 0.55 m s^{-1} to 3.3 m s^{-1}. This affects the dynamics of liquid water especially at the interface of the channel and GDL. This can be realized from the convection term, $\varepsilon\lambda_l\rho\vec{V}$ in the conservation equation for liquid water (Eq. (4)). The liquid water velocity (toward the channel) and gas phase velocity (toward the CL) are increased when the mixture velocity is increased. Consequently, more liquid water will be discharged into the channel. This leads to an enhancement in the liquid water removal out of the GDL. It is proposed here, in the gas purge process at shut down when the remained liquid water should be removed from the GDL and channel, both supplying low humidity inlet flow into the channel and increasing the inlet gas flow rate are applicable. Furthermore, at the higher mass flow rate the removal of heat is eased, therefore con-

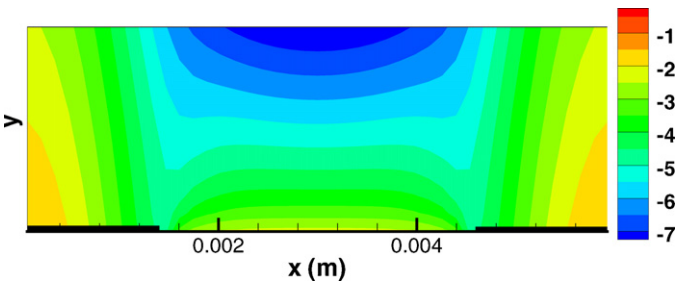

Fig. 10. Through-plane distribution of interfacial phase-change rate (kg m^{-3} s^{-1}) in the cathode GDL when $T = 353$ K, $\phi = 10\%$, and $q = 50 \times 10^{-7}$ m^3 s^{-1}.

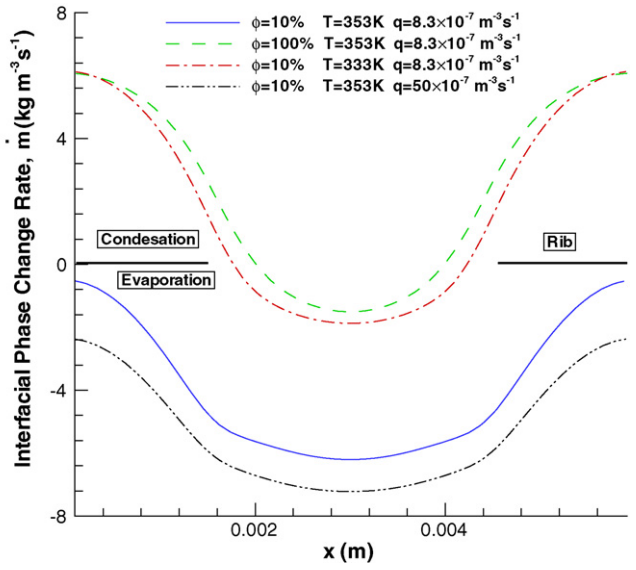

Fig. 11. In-plane profiles of interfacial phase-change rate ($\mathrm{kg\,m^{-3}\,s^{-1}}$) near the CL with $Y^* = y/y_L = 0.9$ where y_L is the GDL height for different parametric conditions.

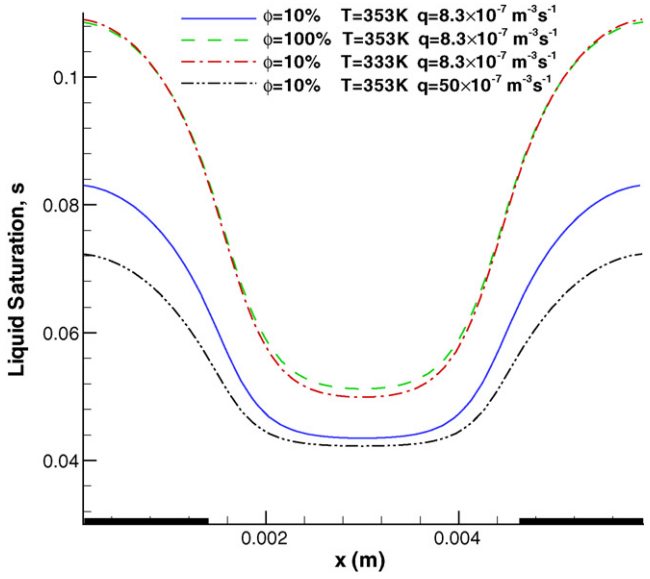

Fig. 12. In-plane profiles of liquid saturation near the CL with $Y^* = y/y_L = 0.9$ where y_L is the GDL height for different parametric conditions.

densation rate is expected to rise. However, the evaporation rate increases and it may result in dehydration of GDL. The reason is the reduced water vapor partial pressure, when the total pressure does not change significantly and the reactant, oxygen gas partial pressure increases.

The effects of each parametric condition (inlet humidity, operating temperature, and inlet gas flow rate) on phase-change rate are addressed separately. In Fig. 11, a summary has been demonstrated by comparing the in-plane profiles of interfacial mass transfer phase-change rate at the different parametric conditions. The in-plane profiles are plotted at $Y^* = 0.9$ which is near the CL. It is seen that the phase-change rate strongly depends on these parameters. The condensation rate increases with higher inlet humidity and lower operating temperature. Moreover, it widens the area under the condensation. On the other hand, the evaporation rate increases when the inlet gas flow rate increases and the inlet relative humidity decreases. Fig. 11 also shows the highest condensation and evaporation rates above the ribs and channel, respectively.

In order to illustrate the most significant effect of the phase changes on the liquid saturation and temperature distribution, for Fig. 11 the corresponding in-plane liquid saturation and local temperature profiles are depicted in Figs. 12 and 13.

Fig. 12 shows the in-plane profiles of the liquid saturation at the different parametric conditions. With the fixed total flux of liquid water entering from CL/GDL interface into the GDL for all four different parametric conditions, the amount of liquid saturation is different. In the cases of higher inlet humidity, $\phi = 100\%$, and lower operating temperature, $T = 333$ K, the liquid saturation is higher compared to lower inlet humidity, $\phi = 10\%$, higher operating temperature, $T = 353$ K, and higher mass flow rate, $q = 50 \times 10^{-7}\,\mathrm{m^3\,s^{-1}}$ (300 sccm). This is due to the corresponding phase-change. In the first two cases, condensation is the dominant phase change (see Fig. 11) where more water vapor is changed to liquid water, therefore the liquid saturation level increases. For the latter three cases, evaporation is the dominant phase change throughout the GDL. Therefore, more liquid water is changed to water vapor and liquid saturation level decreases.

Fig. 13 displays the in-plane profiles of the temperature at the different parametric conditions. The temperature variation is higher in cases of the higher inlet humidity, $\phi = 100\%$, and lower operating temperature, $T = 333$ K. Again, the reason is attributed to the corresponding phase-change. From Fig. 11, the dominant phase change in these cases is condensation, therefore the latent heat of vapor–liquid (water) phase change is released. This leads to to the higher temperature variation. When evaporation is the dominant phase change (see Fig. 11), a part of the heat produced in the CL entering from the GDL/CL interface is absorbed for vaporization. This reduces the temperature variation inside the domain.

It is interesting to note that for all the different parametric conditions, the local temperature is higher above the channel compared to above the ribs. This temperature gradient creates thermal diffusion of the vapor phase from the hotter area to the colder area. Water vapor is then condensed above the ribs and increases the liquid saturation. This phenomenon is termed as the heat pipe effect [9] or phase change induced flow [24]. The effects of this phenomenon can be seen in Figs. 11 and 12 where the condensation rate and liquid saturation are increased above the ribs. Furthermore, it is seen that the heat pipe effects is stronger in case of the higher inlet humidity and lower operating temperature.

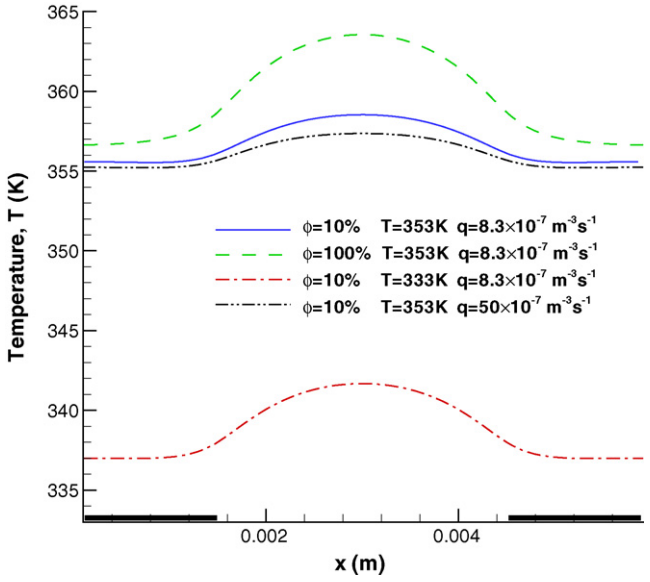

Fig. 13. In-plane profiles of temperature (K) near the CL with $Y^* = y/y_L = 0.9$ where y_L is the GDL height for different parametric conditions.

6. Conclusion

In this paper, a three-dimensional two-phase non-isothermal numerical study with effects of non-equilibrium phase change rates showed the role of the phase-change rate on fuel cell operation. It was shown that the maximum evaporation rate zone coincides with the maximum temperature and lowest liquid saturation zones. On the other hand, the maximum condensation zone coincides with the lowest temperature and highest saturation zone. The difference of liquid or vapor phases assumption for the water produced in the CL, aside from the transient response, was found to be the different local distribution of evaporation–condensation rate. The parametric studies also showed that (i) condensation interfacial phase change rate increases with increasing the channel inlet humidity and decreasing operation temperature and (ii) evaporation interfacial phase change rate increases with reduction the channel inlet humidity and an increase the inlet mass flow rate. In-plane profiles of phase-change rate showed the maximum condensation rate above and near the ribs and maximum evaporation rate above the channel near the CL.

Acknowledgements

This work has been partly supported by the ENERGY-GCOE program at Tokyo Institute of Technology and the NEDO Robust Project.

References

[1] C.Y. Wang, P. Cheng, Int. J. Heat Mass Transfer 39 (1996) 3607–3618.
[2] V. Gurau, H. Liu, S. Kakac, AIChE J. 44 (1998) 2410–2422.
[3] Z.H. Wang, C.Y. Wang, K.S. Chen, J. Power Sources 94 (2001) 40–50.
[4] L. You, H. Liu, Int. J. Heat Mass Transfer 45 (2002) 2277–2287.
[5] J.H. Nam, M. Kaviany, Int. J. Heat Mass Transfer 46 (2003) 4595–4611.
[6] U. Pasaogullari, C.Y. Wang, J. Electrochem. Soc. 151 (2004) A399–A406.
[7] E. Birgersson, M. Noponen, M. Vynnycky, J. Electrochem. Soc. 152 (2005) A1021–A1034.
[8] H. Meng, C.Y. Wang, J. Electrochem. Soc. 152 (2005) A1733–A1741.
[9] Y. Wang, C.Y. Wang, J. Electrochem. Soc. 153 (2006) A1193–A1200.
[10] F.Y. Zhang, X.G. Yang, C.Y. Wang, J. Electrochem. Soc. 153 (2006) A225–A232.
[11] D. Song, Q. Wang, Z.S. Liu, C. Huang, J. Power Sources 159 (2006) 928–942.
[12] Y. Shan, S.Y. Choe, S.H. Choi, J. Power Sources 165 (2007) 196–209.
[13] G. Hu, J. Fan, J. Power Sources 165 (2007) 171–184.
[14] H. Wu, P. Berg, X. Li, J. Power Sources 165 (2007) 232–243.
[15] H. Meng, J. Power Sources 168 (2007) 218–228.
[16] H. Ju, G. Luo, C.Y. Wang, J. Electrochem. Soc. 154 (2007) B218–B228.
[17] G. Luo, H. Ju, C.Y. Wang, J. Electrochem. Soc. 154 (2007) B316–B321.
[18] Y. Wang, C.Y. Wang, J. Electrochem. Soc. 154 (2007) B636–B643.
[19] N. Djilali, Energy 32 (2007) 269–280.
[20] P.K. Sinha, C.Y. Wang, J. Power Sources 183 (2008) 609–618.
[21] Y. Wang, J. Power Sources 185 (2008) 261–271.
[22] M. Khakbaz Baboli, M.J. Kermani, Electrochim. Acta 53 (2008) 7644–7654.
[23] Y. Wang, S. Basu, C.Y. Wang, J. Power Sources 179 (2008) 603–617.
[24] M. Khandelwal, S. Lee, M.M. Mench, J. Electrochem. Soc. 156 (2009) B703–B715.
[25] S. Basu, C.Y. Wang, K.S. Chen, J. Electrochem. Soc. 156 (2009) B748–B756.
[26] H. Wu, X. Li, P. Berg, Appl. Energy, doi:10.1016/j.apenergy.2009.06.024, in press.
[27] H. Wu, X. Li, P. Berg, Electrochim. Acta 54 (2009) 6913–6927.
[28] J.H. Nam, K.J. Lee, G.S. Hwang, C.J. Kim, M. Kaviany, Int. J. Heat Mass Transfer 52 (2009) 2779–2791.
[29] N. Khajeh-Hosseini-Dalasm, M.J. Kermani, D. Ghadiri Moghaddam, J.M. Stockie, Int. J. Hydrogen Energy 35 (2010) 2417–2427.
[30] N. Khajeh-Hosseini-Dalsam, K. Fushinobu, K. Okazaki, Int. J. Hydrogen Energy 35 (2010) 4234–4246.
[31] S.V. Patankar, Numerical Heat Transfer and Fluid Flow, Hemisphere Publishing Corp. McGraw-Hill, 1984.
[32] H. Versteeg, W. Malalasekra, An Introduction to Computational Fluid Dynamics: The Finite Volume Method, Prentice Hall, 1995.